



Point Defects and Localized Excitons in 2D WSe₂

Item Type	Article
Authors	Zheng, Yu Jie;Chen, Yifeng;Huang, Yu Li;Gogoi, Pranjal Kumar;Li, Ming-yang;Li, Lain-Jong;Trevisanutto, Paolo E.;Wang, Qixing;Pennycook, Stephen J.;Wee, Andrew T. S.;Quek, Su Ying
Citation	Zheng, Y. J., Chen, Y., Huang, Y. L., Gogoi, P. K., Li, M.-Y., Li, L.-J., ... Quek, S. Y. (2019). Point Defects and Localized Excitons in 2D WSe ₂ . ACS Nano, 13(5), 6050–6059. doi:10.1021/acsnano.9b02316
Eprint version	Post-print
DOI	10.1021/acsnano.9b02316
Publisher	American Chemical Society (ACS)
Journal	ACS Nano
Rights	This document is the Accepted Manuscript version of a Published Work that appeared in final form in ACS Nano, copyright © American Chemical Society after peer review and technical editing by the publisher. To access the final edited and published work see http://pubs.acs.org/doi/10.1021/acsnano.9b02316 .
Download date	2024-04-17 07:52:37
Link to Item	http://hdl.handle.net/10754/668373

Supplementary Information for:

Point Defects and Localized Excitons in 2D WSe₂

Yu Jie Zheng^{1,2, †}, *Yifeng Chen*^{2, †}, *Yu Li Huang*^{1,3}, *Pranjal Kumar Gogoi*¹, *Ming-Yang Li*⁴,
*Lain-Jong Li*⁴, *Paolo E. Trevisanutto*², *Qixing Wang*¹, *Stephen J. Pennycook*^{5,*}, *Andrew T. S.*
Wee^{1,2,*}, *Su Ying Quek*^{1,2,*}

¹Department of Physics, National University of Singapore, 2 Science Drive 3, 117551,
Singapore

²Centre for Advanced 2D Materials, National University of Singapore, Block S14, Level 6, 6
Science Drive 2, 117546, Singapore

³Institute of Materials Research & Engineering (IMRE), A*STAR (Agency for Science,
Technology and Research), 2 Fusionopolis Way, Innovis, 138634, Singapore

⁴Physical Sciences and Engineering, King Abdullah University of Science and Technology,
Thuwal, 23955-6900, Saudi Arabia

⁵Department of Materials Science & Engineering, National University of Singapore, 9
Engineering Drive 1, Singapore 117575

†: These authors contributed equally to this work.

Corresponding Authors *: phyqsy@nus.edu.sg (theory); phyweets@nus.edu.sg (STM);
msepsj@nus.edu.sg (STEM)

METHODS

1. Density Functional Theory (DFT) calculations 3
2. Chemical Vapor Deposition (CVD) 5
3. Scanning tunneling microscopy/spectroscopy (STM/S) 5
4. Scanning Transmission Electron Microscopy (STEM) 5

FIGURES

- FIG. S1. Formation energies of intrinsic defects. 7
- FIG. S2. Side view of the intrinsic point defects in WSe₂ ML on graphite. 8
- FIG. S3. PDOS on the intrinsic defect sites in WSe₂ ML on graphite. 9
- FIG. S4. Atomic structure and DOS for the final state in Figure 2a of the main text. 10
- FIG. S5. O₂ dissociative adsorption at the Se vacancy site. 11
- FIG. S6. STM/S results for perfect SL-WSe₂ on graphite. 12
- FIG. S7. STM images for D₂, compared with simulated STM images for O_{ins} and O_{Se-down} (O substituting the bottom Se atom). 13
- FIG. S8. Simulated STM images of the intrinsic defects in SL-WSe₂ on graphite. 14
- FIG. S9. HAADF STEM image at 60 kV accelerating voltage together with intensity analysis. 15
- FIG. S10. Charge density plots for DFT eigenfunctions at the K point, in the 4 x 4 supercell with O_{ins}. 16
- FIG S11. (a) GW and (b) DFT-SOC band structure with m_z projection for 4x4 supercell with O_{Se} defect. 17
- FIG S12. (a) GW and (b) DFT-SOC band structure with m_z projection for 4x4 supercell with Se_w defect. 17
- FIG. S13. GW-BSE absorption spectra with spin orbit coupling applied perturbatively. 18
- FIG S14. RPA spectra without SOC for 7x7 supercell of (a) O_{ins}, (b) O_{Se}, and (c) Se_w anti-site defect. 19
- FIG S15: STM images simulated with HSE06 functional. 20
- FIG. S16: DFT-PBE band structure of O_{ins} defective system in 4x4 and 7x7 supercells. 20
- FIG. S17: SOC effects on the electronic and optical spectra of pristine WSe₂ 21

TABLES:

- Table S1. Formation energies of selected defects in WSe₂. 7
- Table S2. Formation energies in eV of selected defects in isolated MoS₂ ML. 8
- Table S3. Energy barrier for dissociation of O₂ on Se_{vac} in WSe₂, computed for different exchange-correlation functionals. 10
- Table S4. Binding energies (E_b) of the O atoms in the final state. 11
- Table S5. Analysis of exciton wavefunctions. 16

METHODS

1. Density Functional Theory (DFT) calculations

Electronic Properties of Defects

Except for the calculations for optical properties, the density functional theory (DFT) calculations in this manuscript were performed with the VASP code¹ using the PAW approach and a kinetic energy cutoff of 400 eV. We use the PBE exchange-correlation functional² with Grimme's D2³ correction for van der Waals (vdW) interactions for all calculations except the density of states (DOS) plots which were performed with the hybrid HSE06⁴ exchange-correlation functional. Spin polarization is included for the defect structures and for oxygen. Geometry optimization is performed with a force convergence criteria of 0.01 eV/Å for single layer (SL)-WSe₂, and 0.05 eV/Å for SL-WSe₂ supported on graphite. The lattice constant is fixed to that optimized for the pristine WSe₂ layer, which compares well to experimental values. The total energy of bulk WSe₂ is converged for the chosen energy cutoff, as well as with a Monkhorst Pack k-grid sampling of 10 × 10 × 4 in the bulk WSe₂ unit cell. SL-WSe₂ on graphite was modeled using 3 layers of graphite, with a 3 × 3 WSe₂ supercell on top of a 4 × 4 supercell of graphite and 13 Å of vacuum. In this supercell, the strain on WSe₂ was 0.61 % and the strain on graphite was -0.65 %. Defects in SL-WSe₂ on graphite were studied using a 2×√3R30° supercell of the WSe₂/graphite supercell described above. In these defect supercells, we used a k-mesh of 2 × 2 × 1 for geometry optimization and 4 × 4 × 1 for DOS calculations. For defects in isolated WSe₂, we used a 5 × 5 supercell, with a 2 × 2 k-mesh for geometry optimization and a 6 × 6 k-mesh for DOS calculations.

The formation energy of the (charge neutral) defects is defined as

$$E_f(x) = E(x) - E_{pristine} - \sum_i n_i \mu_i \quad (1)$$

where $E(x, q)$ and $E_{pristine}$ are the total energies of the WSe₂/graphite supercell with and without the defect, respectively. n_i denotes the number of atoms of element i that have been added ($n_i > 0$) or removed ($n_i < 0$), and μ_i is the chemical potential of element i . The chemical potentials of W and Se are linked by the stability of WSe₂, *i.e.*

$$\mu_{WSe_2} = \mu_W + 2\mu_{Se} \quad (2)$$

μ_{WSe_2} is the total energy per formula unit of bulk WSe₂ (the conclusions are unchanged if we use instead the total energy per formula unit of monolayer WSe₂). μ_W^{\max} and μ_{Se}^{\max} are total energies per atom of bcc W metal and the molecular crystal ($R\bar{3}$ phase) of Se₆ molecules, respectively. The minimum of the Se chemical potentials can be derived from formula (2), *i.e.*, $\mu_{Se}^{\min} = (\mu_{WSe_2} - \mu_W^{\max}) / 2$.

For formation energies of oxygen defects in the presence of oxide precursors, we have referred the chemical potential of O to its reservoir WO₃ (P6mmm).

$$\mu_{WO_3} = \mu_W + 3\mu_O \quad (3)$$

Similar formulas are used for the formation energies of the S_{vac}, O_S and O_{ins} defects in MoS₂. The chemical potential of Mo-rich and S-rich referred to Molybdenum (bcc) and Sulphur (alpha phase) crystals. The O chemical potential is taken to be that from MoO₃ (Pbnm).

For the computation of dissociation barriers and rate constants, 5×5 supercells with >15 Å vacuum were used, with a Monkhorst-Pack k-mesh of 2×2×1 and a force convergence criterion of 0.01 eV/Å. The dissociation barrier was computed using the climbing image nudged elastic band (cl-NEB) method⁵. The prefactor of the reaction was estimated within harmonic transition state theory (HTST)⁶⁻⁷, and is given by $A = \frac{\prod_i^{3N} v_i^{IS}}{\prod_i^{3N-1} v_i^{TS}}$, where N is the number of free atoms, v_i^{IS} and v_i^{TS} are stable (real valued) normal mode frequencies at the initial states (IS) and transition states (TS) or saddle point. At the transition state, exactly one of the vibrational modes has an imaginary frequency. From the prefactor A , the rate constant k is obtained by $k = A \exp\left[-\frac{E^{TS} - E^{IS}}{k_B T}\right]$. E^{IS} and E^{TS} are the energies at the initial and transition states. k_B and T are the Boltzmann's constant and temperature, respectively.

Besides using the PBE-D2 functional as described in the main text, we have also computed the O₂ dissociation barriers using the RPBE functional⁸ with and without Grimme's D3 dispersion correction,⁹ and the BEEF-vdW functional.¹⁰ The RPBE functional, when applied to dissociative adsorption of O₂ on Cu surfaces, gave

reasonable agreement with experiment,¹¹ while the BEEF-vdW functional performed well compared to an experimental benchmark database of molecular dissociation barriers on surfaces.¹² The results are shown in Table S1.

DFT band structures with spin orbit coupling (SOC) were also computed using VASP.

Random Phase Approximation (RPA) calculations

RPA calculations were performed with Yambo¹³ using a damping parameter of 0.01 eV. RPA with SOC calculations were performed with spinor wavefunctions using fully relativistic ONCV pseudopotentials. For 4x4 supercells, the response function has a dimension in reciprocal space of 1000 mHa. However, for 7×7 supercells, the corresponding dimension is ~ 0.5 mHa due to the large computational expense.

2. Chemical Vapor Deposition (CVD)

Monolayer WSe₂ was grown directly on graphite and on sapphire substrates by chemical vapor deposition (CVD) as reported in Ref. 14. In brief, high purity WO₃ and Se powders are used as precursors. WO₃ powders were placed in a ceramic boat at the center of a furnace and Se powders were placed at the upstream side, while the graphite or sapphire substrate was positioned in the downstream side next to the WO₃ powders. Ar was used as carrier gas to carry the evaporated Se and WO₃ to the target substrates for reaction. H₂ was added as a reducing agent. STM and STEM confirmed that the samples used were monolayer in thickness.

3. Scanning tunneling microscopy/spectroscopy (STM/S)

STM/S measurements were performed in a custom-built multi-chamber system housing an Omicron LT-STM operating at ~ 77 K under ultrahigh vacuum conditions (10^{-10} mbar). All STM images were recorded in constant current mode with tunneling current in the range 50-100 pA. Differential conductance dI/dV or STS were acquired by a lock-in amplifier with a sinusoidal modulation of 40 mV at 625 Hz. Note that the bias voltage (V_{Tip}) is applied on the STM tip with respect to the sample, hence negative values correspond to empty states and positive values correspond to filled states. Each STS curve was obtained by averaging hundreds

of individual spectra acquired. An electrochemically etched tungsten tip was used in all measurements. Before STM investigations, the *ex-situ* grown sample was degassed at $\sim 300^\circ\text{C}$ overnight to remove adsorbates (*e.g.*, O_2 , H_2O , *etc.*) physisorbed during exposure in ambient conditions.

4. Scanning Transmission Electron Microscopy (STEM)

Transfer to TEM grid:

At first, the WSe_2 /sapphire sample surface was spin-coated with poly(methyl methacrylate) (PMMA, A4, 950 K in anisole, MicroChem) at 4000 rpm for 60 second. After curing the spin-coated sample at 100°C for 10 min, the edges of the sample were scratched, so that the etching agent can easily reach the WSe_2 -sapphire interface. The sample was then floated on NaOH (3M) etching solution to separate the PMMA coated WSe_2 film from the sapphire substrate. After separation, the floating film was transferred to DI water beakers a few times consecutively and later fetched using a quantifoil copper TEM grid. The TEM grid with PMMA-coated WSe_2 film was thereafter heated at 100°C for 5 min to get better adhesion and to remove water. The PMMA coating was washed off finally, using acetone and IPA. This transfer process was carried out inside a class 1000 cleanroom in Singapore Synchrotron Light Source (SSLS) situated at the National University of Singapore (NUS) campus.

Scanning Transmission Electron Microscopy:

Aberration-corrected scanning transmission electron microscopy (STEM) images were taken at 60 kV accelerating voltage using the JEOL ARM200 F installed inside SSLS, NUS. The microscope, with 80 pm resolution at 200 kV and demonstrated information transfer of 95 pm at 40 kV, is capable of high-resolution imaging to reveal the atomic structure and defects. The lower accelerating voltage of 60 kV used here for WSe_2 is much below the knock-on damage threshold of Se and W atoms in WSe_2 , and hence it ensures negligible beam-damage. High-angle annular dark-field (HAADF) image intensities depend on the atomic number of the corresponding atoms in the sample. All the images reported here were taken with the HAADF detector with the collection angle range of 68-280 mrad. The convergence angle of the probe beam was about 30 mrad.

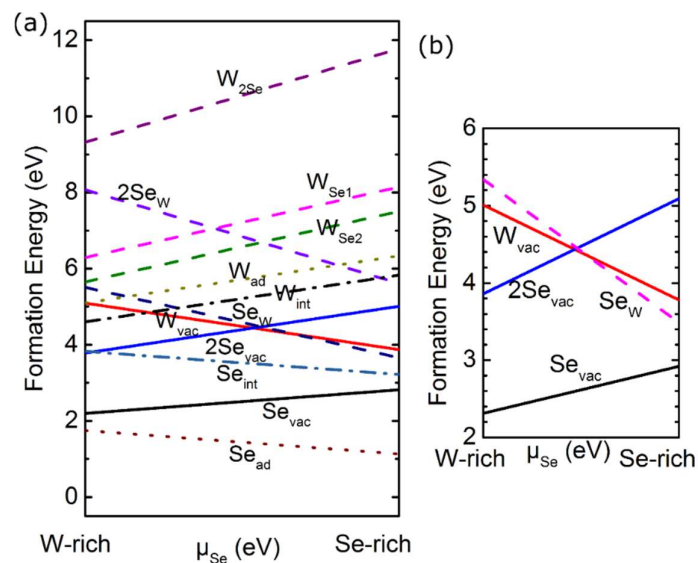


FIG S1. Formation energies of intrinsic defects (a) with and (b) without graphite substrate. Solid lines denote vacancies, dashed lines substitutional (antisite) defects, dotted lines adatoms, and dotted-dashed lines intercalated atoms.

Defect	W-rich conditions		Se-rich conditions	
	Isolated	Supported	Isolated	Supported
Se_{vac}	2.31	2.20	2.92	2.82
W_{vac}	5.01	5.09	3.78	3.87
Se_W	5.34	5.51	3.49	3.66
2Se_{vac}	3.86	3.78	5.09	5.01
O_{Se}	0.52	0.33	0.73	0.53
O_{ins}	2.38	2.36	1.97	1.95
O_{ad}	2.91	2.81	2.50	2.40

Table S1. Formation energies in eV of selected intrinsic defects, and O-related defects in isolated WSe_2 ML and in WSe_2 ML supported on graphite.

Defect	Mo-rich conditions	S-rich conditions
S_{vac}	1.55	2.81
O_S	-0.09	0.33
O_{ins}	3.72	2.88

Table S2. Formation energies in eV of selected defects in isolated MoS_2 ML.

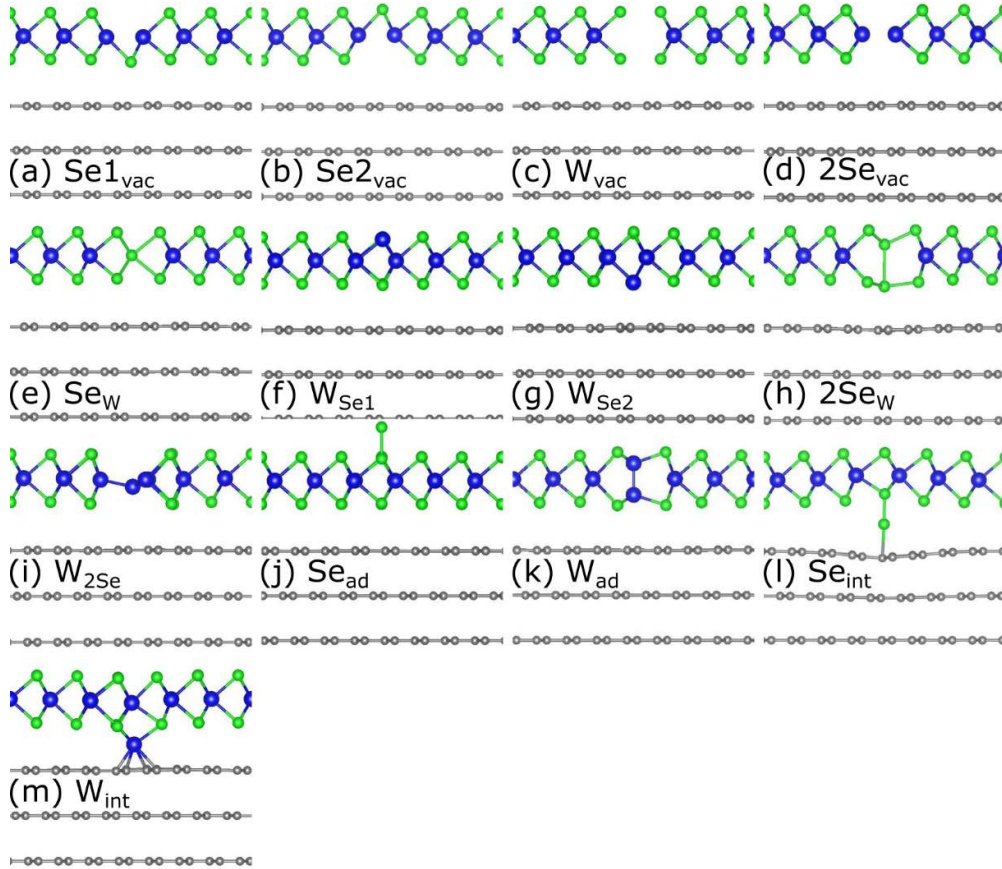


FIG. S2. Side view of the intrinsic point defects in WSe_2 ML on graphite. Blue: W, Green: Se, Gray: C. We note that $W_{\text{Se}2}$ has a slightly smaller formation energy than $W_{\text{Se}1}$. Analysis of the detailed atomic structure indicates that the W-W bonds are $\sim 0.1 \text{ \AA}$ longer in $W_{\text{Se}2}$ than in $W_{\text{Se}1}$, suggesting that interaction with graphite stabilizes the substitutional W atom.

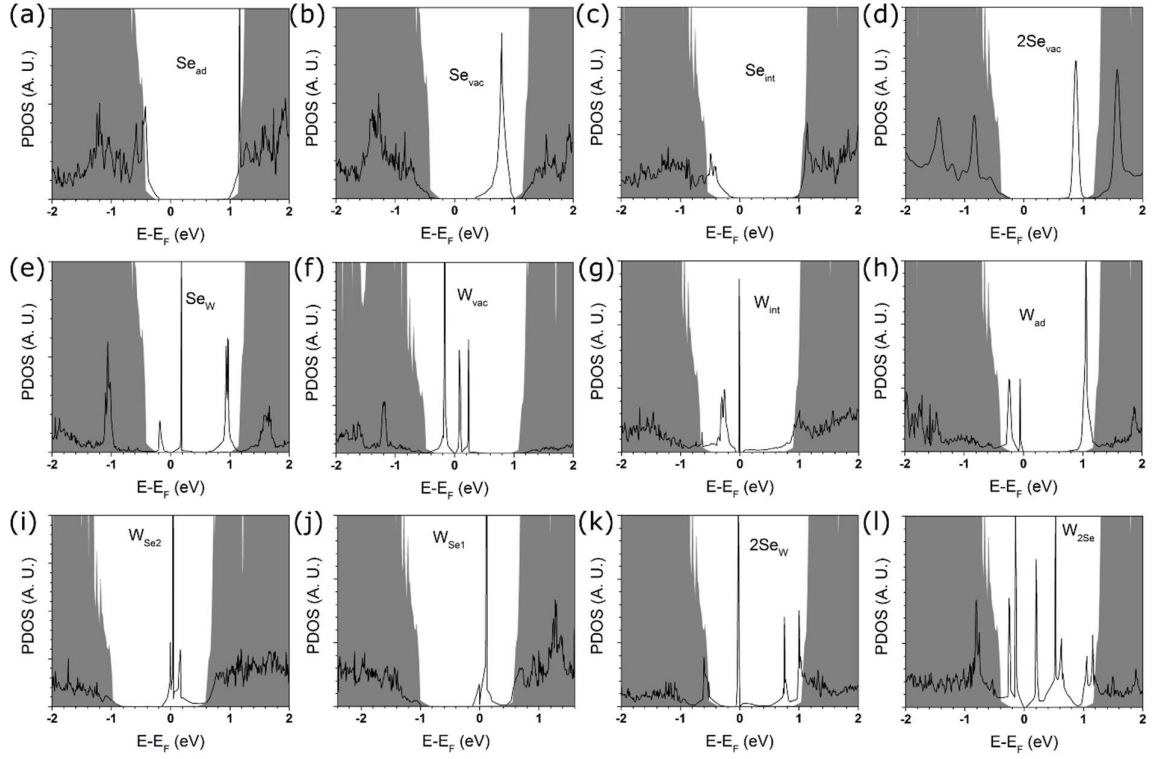


FIG. S3. PDOS (DFT PBE) on the intrinsic defect sites in WSe_2 ML on graphite. Gray shading: PDOS of perfect WSe_2 on graphite. The PDOS with and without defects are aligned by the $1s$ core level of W furthest from the defect site. The Fermi level refers to the Fermi level of WSe_2 ML with defects on graphite.

Table S3. Energy barrier for dissociation of O_2 on Se_{vac} in WSe_2 , computed for different exchange-correlation functionals.

	PBE-D2	PBE-D2 (with zero point correction)	RPBE	RPBE-D3	BEEF-vdW ¹
Barrier (eV)	0.52	0.48	0.54	0.57	0.51

- For BEEF-vdW, the number in the table is obtained from structures where the lattice constant is fixed to that of PBE-D2, which is closer to experiment. Using the lattice constant optimized with BEEF-vdW (overestimated by $\sim 3.5\%$), we obtain a much smaller energy barrier of 0.13 eV.

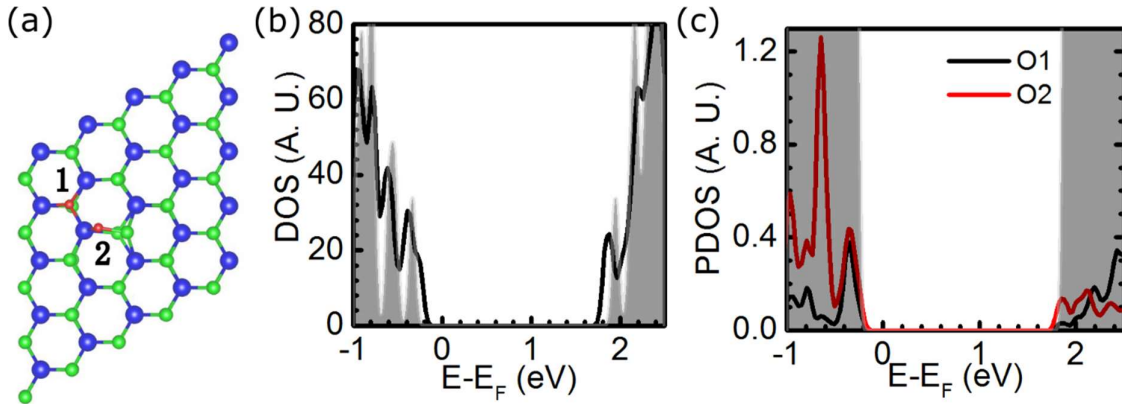


FIG. S4. Atomic structure and DOS for the final state in Figure 2a of the main text. (a) Top view of atomic structure (Blue: W, Green: Se, Red: O), (b) DOS of final state, (c) PDOS on the O atoms which are marked in (a). Gray shading represents the DOS of perfect WSe_2 , aligned using the 1s levels of W atoms furthest from the defect.

Table S4. Binding energies (E_b) in eV of the O atoms in the final state. $E_b = E_{2O} - E_{1O} - \mu_O$, where E_{2O} is the total energy of the final state in Figure 2a, E_{1O} is the total energy after the specified O atom is removed, and μ_O is half of the total energy of O_2 , and for the number in brackets, μ_O is the energy of atomic O. Spin polarization is included. We see that the O1 atom is much more strongly bound than O2.

	O1	O2
E_b	-4.2 (-6.8)	0.3 (-2.3)

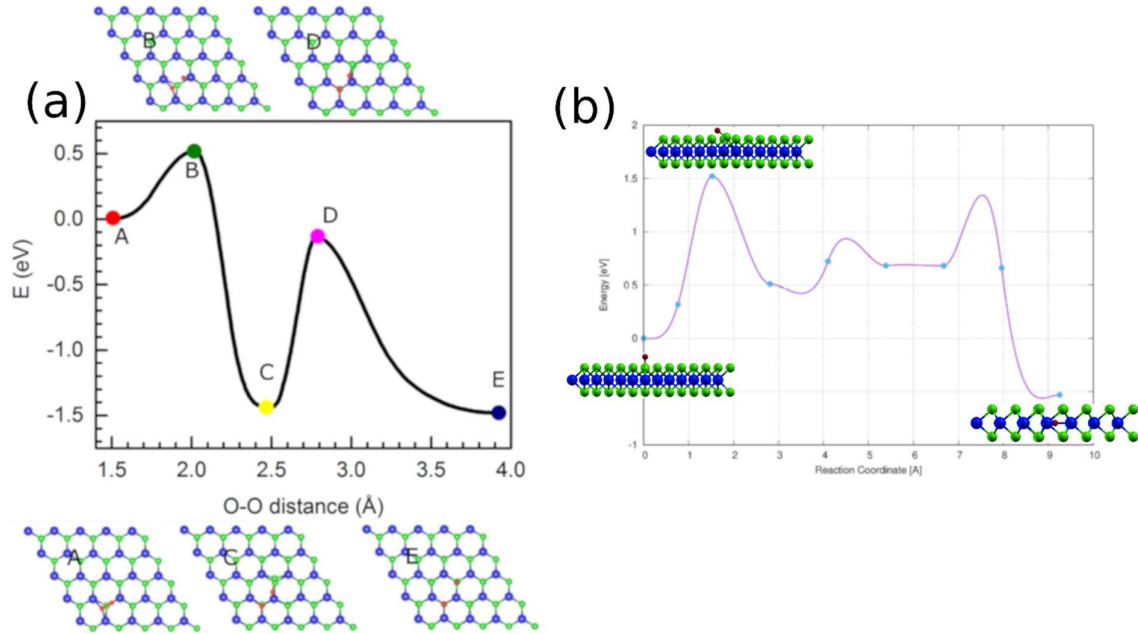


FIG. S5. (a) O_2 dissociative adsorption at the Se vacancy site and diffusion of oxygen atom to O_{ad} ; (b) Energy barrier for O atom to diffuse from O_{ad} to O_{ins} . The energy barrier from O_{ad} to O_{ins} is 1.5 eV, smaller than the binding energy of O atoms (relative to atomic O) at the different binding sites.

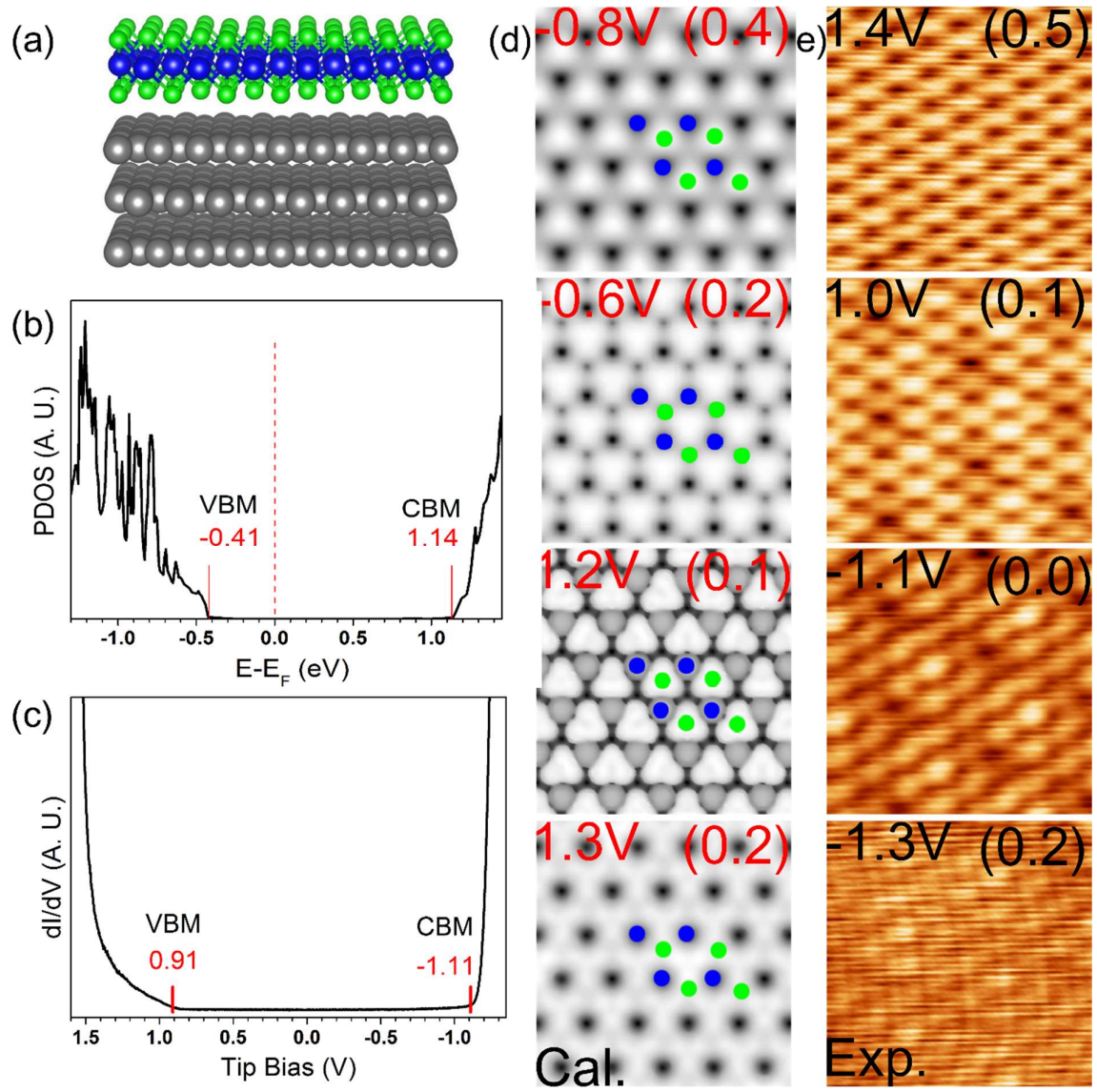


FIG. S6. STM/S results for perfect SL-WSe₂ on graphite. (a) Atomic structure. (Blue: W; Green: Se; Gray: C) (b) PDOS (PBE) of WSe₂ on graphite reveals a 1.55 eV band gap. (c) STS spectrum reveals a 2.02 eV bandgap for SL-WSe₂ ($V_{\text{Tip}}=1.3$ V, 68.5 pA) on graphite with slight p-type doping characteristic, similar to previous reports.¹⁵ (d) Simulated STM images at different bias voltage (values in parenthesis referenced to the band edges) with atoms overlain in the images (Blue spots: W, Green spots: Se). Energy ranges chosen for the simulation approximate those in the experiment. (e) Bias dependent experimental STM images of SL-WSe₂ on graphite (values in parenthesis referenced to band edges).

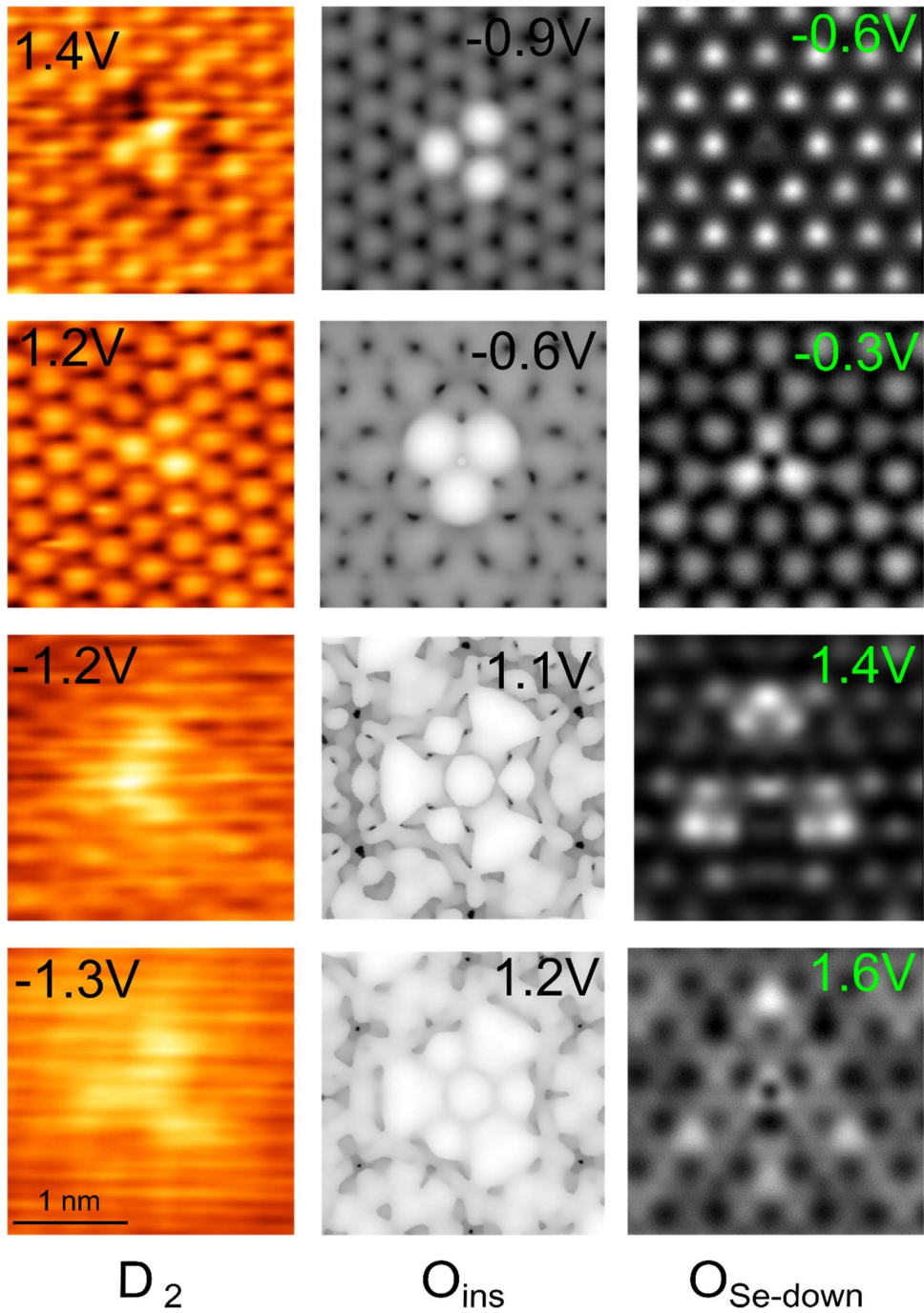


FIG. S7. STM images for D_2 , compared with simulated STM images for O_{ins} and $O_{Se-down}$ (O substituting the bottom Se atom)

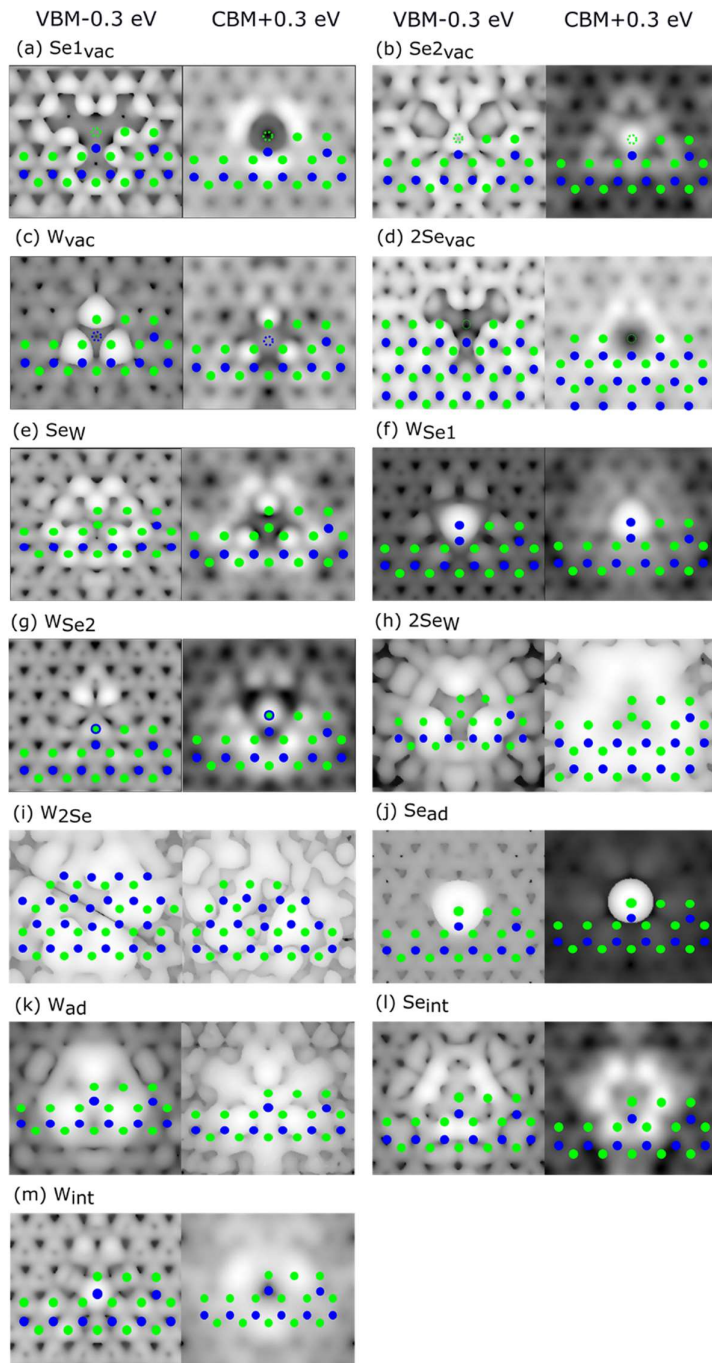


FIG. S8. Simulated STM images of the intrinsic defects in SL-WSe₂ on graphite. The energy ranges are chosen to probe occupied and unoccupied states that are 0.3 eV away from the band edges. Atomic positions are overlain on the images. Blue: W, Green: Se. Se1_{vac} and Se2_{vac} refer to single Se vacancies with the missing Se being in the top and bottom layer, respectively.

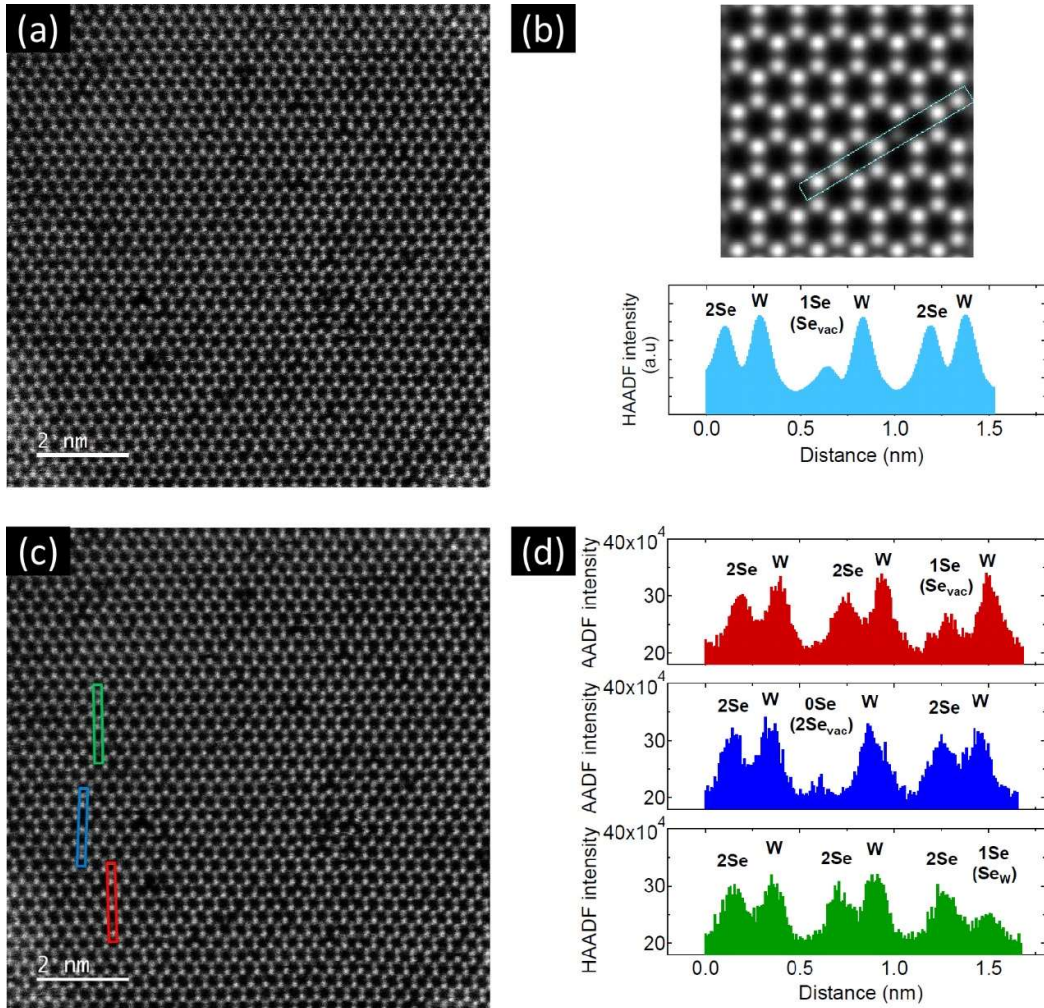


FIG. S9. HAADF STEM image at 60 kV accelerating voltage together with intensity analysis. (a) Raw experimental HAADF STEM image presented in the main text Fig. 4 (g) and (h) (no overlaid atoms now) is shown. (b) Simulated HAADF STEM image and intensity profile, obtained using QSTEM simulation package with input parameters same as in experiments, are shown for the representative case of a region with one Se_{vac} . The brighter spots are due to W atoms and the lesser intensity ones are due to two Se atoms at the Se site. One Se_{vac} is in the simulated image as can be seen in the line profile. The Se_{vac} can be easily distinguished both in the simulated image as well in the line profile due to its reduced intensity. (c) The same experimental HAADF STEM image as in (a) is shown now with line profiles indicated. The red line profile captures a Se_{vac} , the blue line profile captures a 2Se_{vac} , and the green line profile captures a Se_{w} . (d) The corresponding intensity line profiles are plotted for the regions indicated in (c). These experimental line profile intensities (taking the background also into consideration) are used to distinguish the nature of defects by comparing them with corresponding simulated image intensities quantitatively.

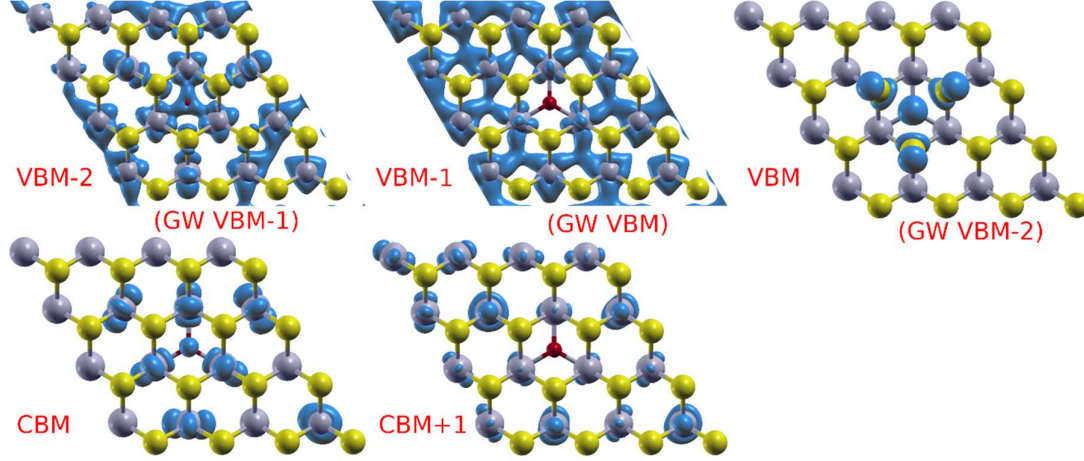


FIG. S10. Charge density plots for DFT eigenfunctions at the K point, in the 4 x 4 supercell with O_{ins} . The isovalue is set to 10% of the maximum of the respective charge distribution, except for VBM, which is set to 1% for better visualization.

LX1: 1.783 eV	CBM	CBM+1	CBM+2	LX2: 1.860 eV	CBM	CBM+1	CBM+2
VBM	0.00006	0.00000	0.00000	VBM	0.00002	0.00001	0.00000
VBM-1	0.88401	0.04781	0.00448	VBM-1	0.41199	0.11755	0.00366
VBM-2	0.02064	0.00593	0.00147	VBM-2	0.40391	0.00617	0.00269
LX3: 1.880 eV	CBM	CBM+1	CBM+2	A: 1.978 eV	CBM	CBM+1	CBM+2
VBM	0.00065	0.00002	0.00000	VBM	0.00036	0.00015	0.00002
VBM-1	0.66412	0.08961	0.00271	VBM-1	0.23457	0.42535	0.01096
VBM-2	0.17760	0.00832	0.00434	VBM-2	0.19933	0.02762	0.01315

Table S5: Analysis of exciton wavefunction for first few bright exciton states in the 4x4 supercell with O_{ins} . The numbers shown are $\sum_{\vec{k}} A_{vc\vec{k}}^S$ for each combination of valence state v

and conduction state c , where the exciton wavefunction is given as $\Psi^S(\vec{r}_e, \vec{r}_h) = \sum_{vc\vec{k}} A_{vc\vec{k}}^S \psi_{c\vec{k}}(\vec{r}_e) \psi_{v\vec{k}}(\vec{r}_h)$. Major contributing entries are highlighted in red. It is

important to note that the GW self-energy corrections result in a reordering of the valence states at the K point. In Table S5, all states are labeled according to the energy ordering in the mean-field DFT (PBE) calculation. At the K point, the DFT states VBM, (VBM-1) and (VBM-2) correspond, respectively, to the GW (VBM-2), GW VBM and GW (VBM-1).

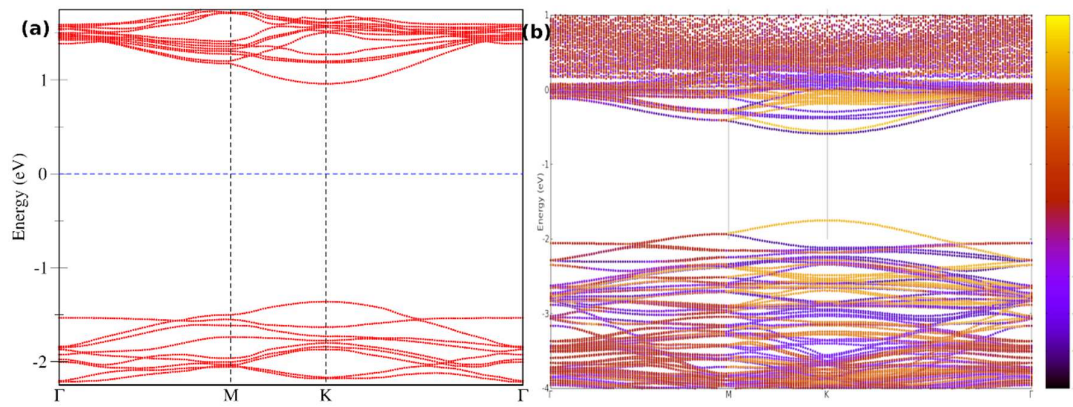


FIG S11. (a) GW and (b) DFT-SOC band structure with m_z projection for 4x4 supercell with O_{Se} defect.

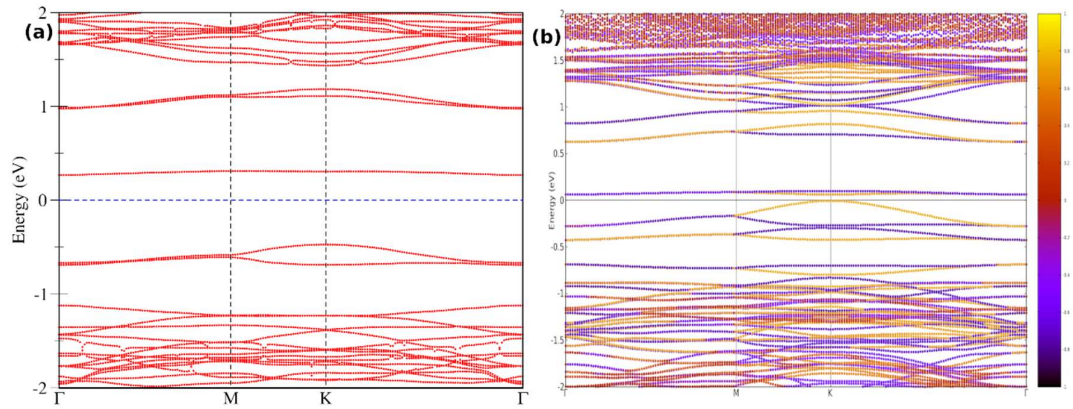


FIG S12. (a) GW and (b) DFT-SOC band structure with m_z projection for 4x4 supercell with Sew defect.

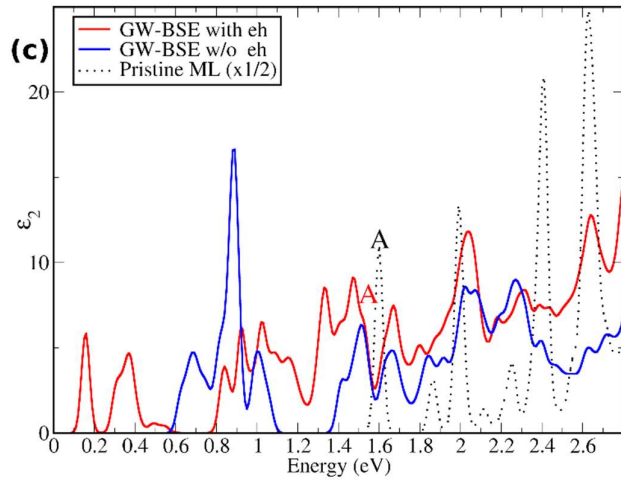
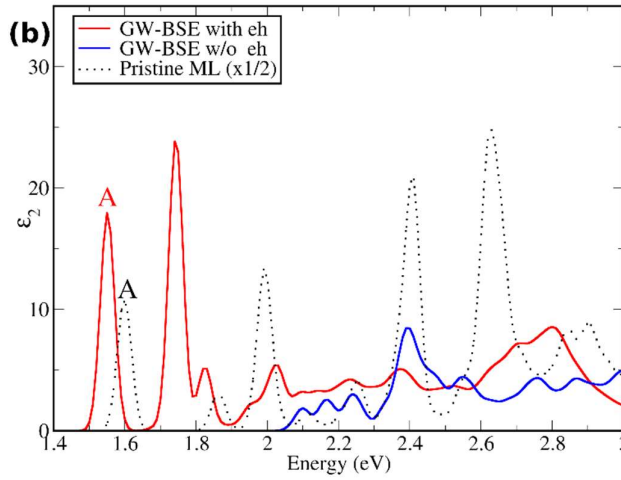
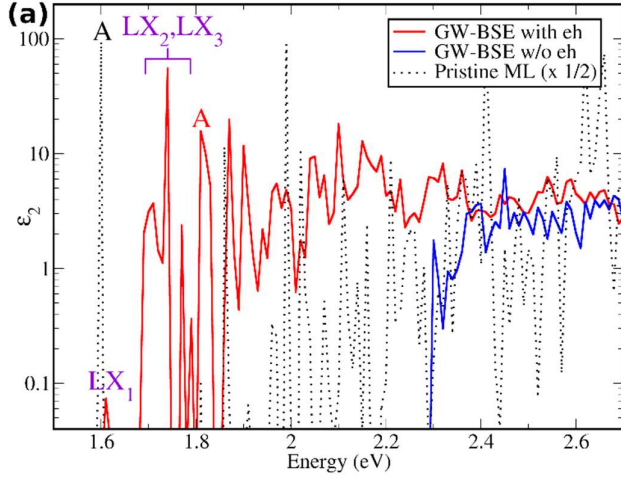


FIG. S13. GW-BSE absorption spectra with spin orbit coupling (SOC) applied perturbatively, for 4x4 WSe₂ supercell with (a) O_{ins}, (b) O_{Se} and (c) S_W defect. SOC is also applied perturbatively for the independent particle absorption spectra (blue) and for the pristine WSe₂ monolayer (black dashed). We note that one should focus only on peaks with energies not larger than the free exciton A peaks in each system.

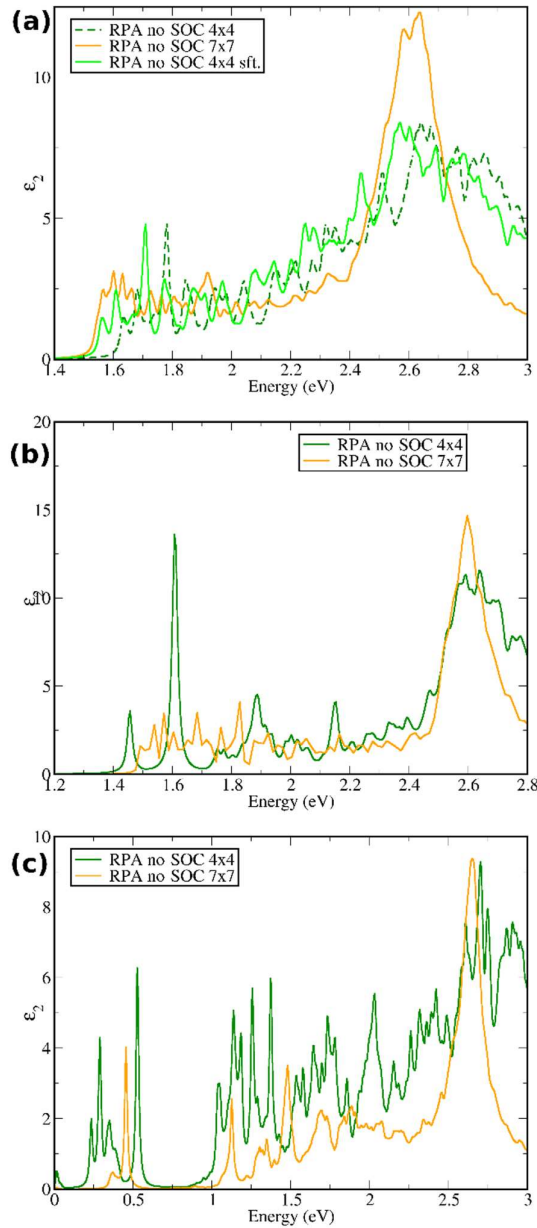


FIG S14. RPA spectra without SOC for 7x7 supercell of (a) O_{ins} , (b) O_{Sc} , and (c) Se_w anti-site defect, in comparison with the corresponding 4x4 supercell result. The 0.072 eV red shifted 4x4 spectrum in (a) is to account for the DFT gap size difference between 4x4 and 7x7 supercell systems. The fact that fewer peaks are present in the 7x7 supercells may be related to the limited number of valence and conduction bands in these calculations.

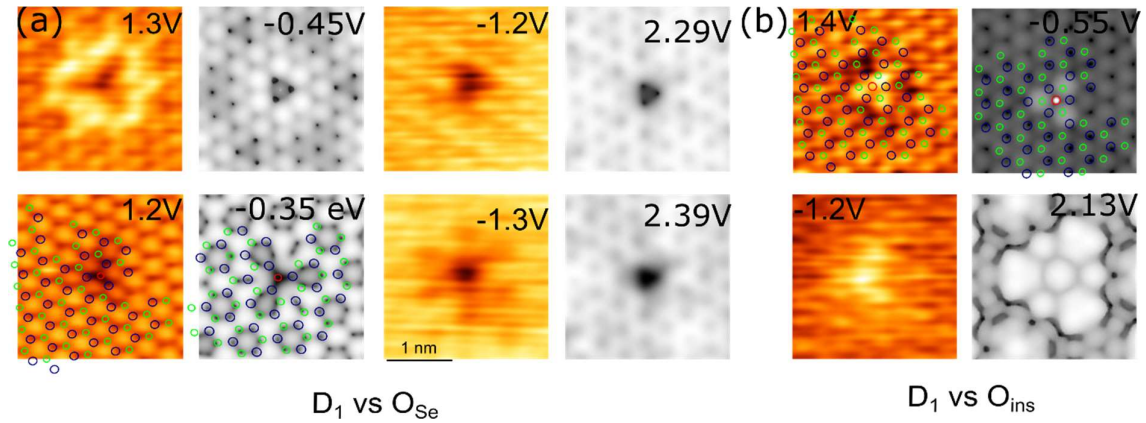


FIG. S15. STM images simulated with HSE06 functional. Left: Experimental STM (Omicron LT-STM operating at ~ 77 K and 10^{-10} mbar) images for (a) D₁ and (b) D₂. Right: Simulated STM images of (a) O_{Se} and (b) O_{ins} using the HSE06 exchange-correlation functional. The atoms are overlain in the images for D1 and D2 defects. (Red: O; Blue: W; Green: Se).

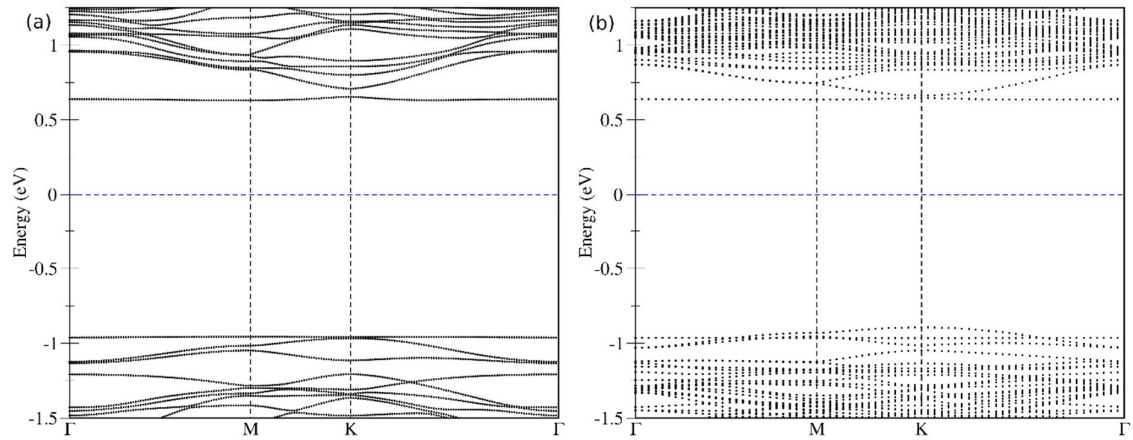


FIG. S16. DFT-PBE band structure of O_{ins} defective system in (a) 4x4 supercell and (b) 7x7 supercell.

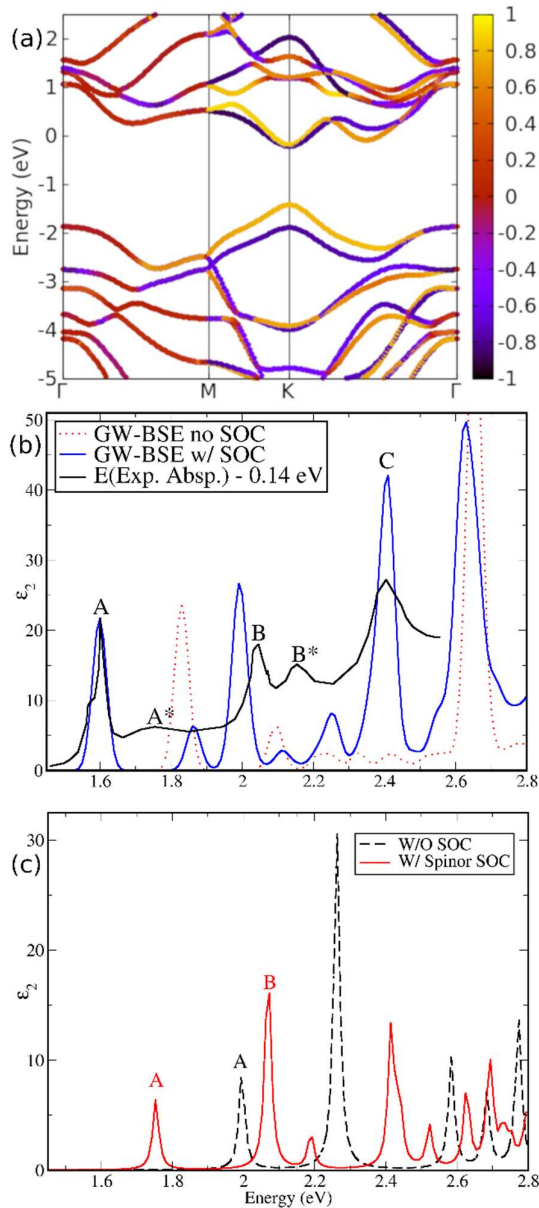


FIG. S17. SOC effects on the electronic and optical spectra of pristine WSe₂ (a) PBE-SOC bandstructure of primitive cell pristine monolayer WSe₂, with m_z value encoded in the color depth scale. (b) GW-BSE optical absorption spectra of pristine WSe₂ without and with perturbative SOC, in comparison with experimental spectrum (from BerkeleyGW). (c) GW-BSE optical spectra of pristine WSe₂ without and with full spinor SOC from Yambo code. Note that here the two spectra are blue shifted rigidly by the same 0.49 eV amount to match with the experimental A peak value at 1.75 eV, due to the underlying under-converged GW quasiparticle spectrum for these calculations.

REFERENCES

1. Kresse, G.; Furthmüller, J., Efficient Iterative Schemes for *Ab Initio* Total-Energy Calculations Using a Plane-Wave Basis Set. *Phys. Rev. B* **1996**, *54*, 11169-11186.
2. Perdew, J. P.; Burke, K.; Ernzerhof, M., Generalized Gradient Approximation Made Simple. *Phys. Rev. Lett.* **1996**, *77*, 3865-3868.
3. Grimme, S., Semiempirical GGA-Type Density Functional Constructed with a Long-Range Dispersion Correction. *J. Comput. Chem.* **2006**, *27*, 1787-1799.
4. Krukau, A. V.; Vydrov, O. A.; Izmaylov, A. F.; Scuseria, G. E., Influence of the Exchange Screening Parameter on the Performance of Screened Hybrid Functionals. *J. Chem. Phys.* **2006**, *125*, 224106.
5. Henkelman, G.; Uberuaga, B. P.; Jonsson, H., A Climbing Image Nudged Elastic Band Method for Finding Saddle Points and Minimum Energy Paths. *J. Chem. Phys.* **2000**, *113*, 9901-9904.
6. Vineyard, G. H., Frequency Factors and Isotope Effects in Solid State Rate Processes. *J. Phys. Chem. Solids* **1957**, *3*, 121-127.
7. Henkelman, G. Methods for Calculating Rates of Transitions with Application to Catalysis and Crystal Growth. Ph.D. thesis, University of Washington, 2001, Chapter 4, Pages 60-69.
8. Hammer, B.; Hansen, L. B.; Norskov, J. K., Improved Adsorption Energetics Within Density-Functional Theory Using Revised Perdew-Burke-Ernzerhof Functionals. *Phys. Rev. B* **1999**, *59*, 7413-7421.
9. Grimme, S.; Antony, J.; Ehrlich, S.; Krieg, H., A Consistent and Accurate *Ab Initio* Parametrization of Density Functional Dispersion Correction (DFT-D) for the 94 Elements H-Pu. *J. Chem. Phys.* **2010**, *132*, 154104.
10. Wellendorff, J.; Lundgaard, K. T.; Mogelhoff, A.; Petzold, V.; Landis, D. D.; Norskov, J. K.; Bligaard, T.; Jacobsen, K. W., Density Functionals for Surface Science: Exchange-Correlation Model Development with Bayesian Error Estimation. *Phys. Rev. B* **2012**, *85*, 235149.
11. Ramos, M.; Diaz, C.; Martinez, A. E.; Busnengo, H. F.; Martin, F., Dissociative and Non-Dissociative Adsorption of O-2 on Cu(111) and Cu-ML/Ru(0001) Surfaces: Adiabaticity Takes Over. *Phys. Chem. Chem. Phys.* **2017**, *19*, 10217-10221.
12. Sharada, S. M.; Bligaard, T.; Luntz, A. C.; Kroes, G. J.; Norskov, J. K., SBH10: A Benchmark Database of Barrier Heights on Transition Metal Surfaces. *J. Phys. Chem. C* **2017**, *121*, 19807-19815.
13. Marini, A.; Hogan, C.; Grunig, M.; Varsano, D., Yambo: an *Ab Initio* Tool for Excited State Calculations. *Comp. Phys. Comm.* **2009**, *180*, 1392.
14. Huang, J. K.; Pu, J.; Hsu, C. L.; Chiu, M. H.; Juang, Z. Y.; Chang, Y. H.; Chang, W. H.; Iwasa, Y.; Takenobu, T.; Li, L. J., Large-Area Synthesis of Highly Crystalline WSe₂ Mono Layers and Device Applications. *ACS Nano* **2014**, *8*, 923-930.
15. Zheng, Y. J.; Huang, Y. L.; Chenp, Y. F.; Zhao, W. J.; Eda, G.; Spataru, C. D.; Zhang, W. J.; Chang, Y. H.; Li, L. J.; Chi, D. Z.; Quek, S. Y.; Wee, A. T. S., Heterointerface Screening Effects Between Organic Monolayers and Monolayer Transition Metal Dichalcogenides. *ACS Nano* **2016**, *10*, 2476-2484.